Iceland Liechtenstein Norway grants

Working together for a green, competitive and inclusive Europe

UEFISCDI
Executive Agency for Higher Education, Research, Development and Innovation Funding

Toward Large Area Perovskite Solar Cells

(PERLA-PV)

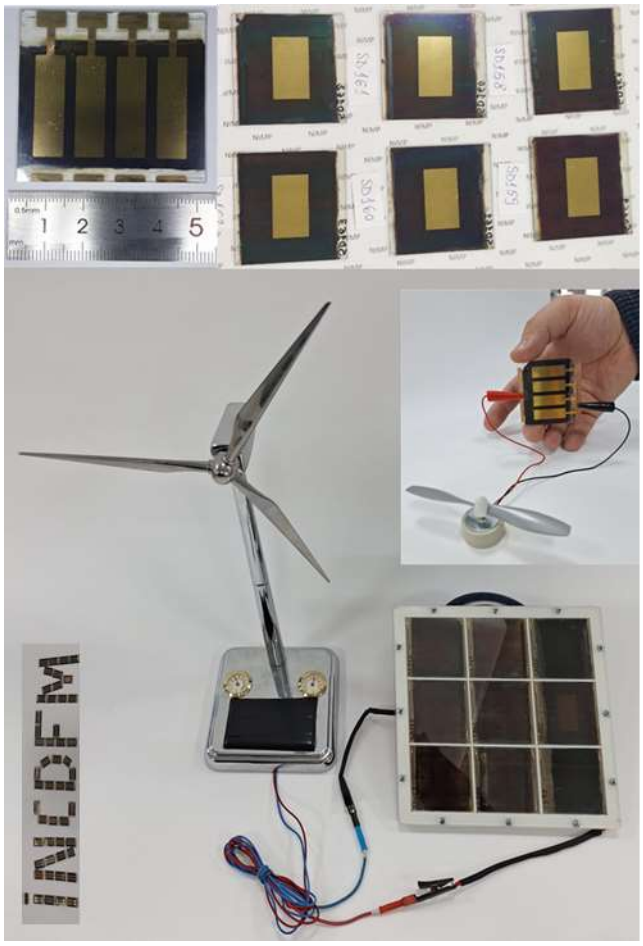

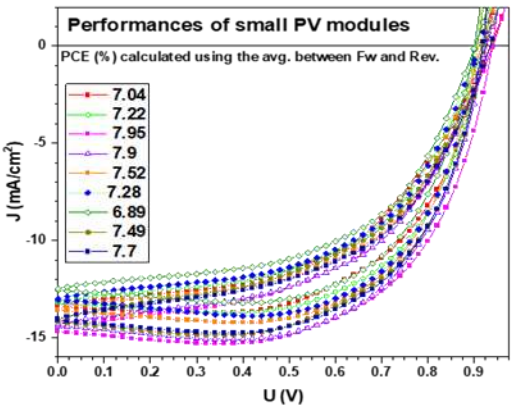

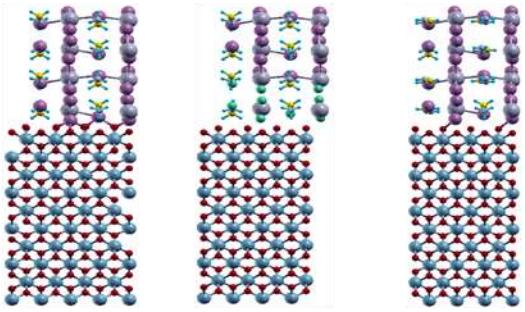

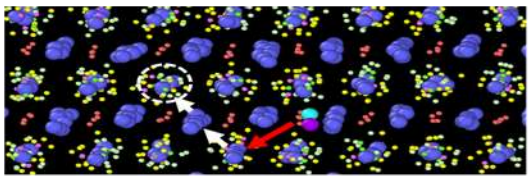

2023

The **PERLA-PV** project started in 2021. It addresses the development of efficient large area perovskite solar cells (PSC) and photovoltaic modules using cheap and environmental friendly technologies. Based on certified record values, as-grown (unstabilized) small area PSCs achieved a power conversion efficiencies over 25%, outperforming some types of Si solar cells, CdTe and CIGS cells. Being also inexpensive to produce, thin, light and suitable for fabrication with printing technologies the PSCs have in principle a great potential for large scale applications and commercialisation. The consortium is composed by 5 partners: project promotor PP - National Institute of Materials Physics (NIMP), P3- *Horia Hulubei National Institute for R&D in Physics and Nuclear Engineering* (IFIN-HH) and P4 - Tritech Group (WATTROM), a SME as end-user, all from Romania; P1- Oslo University (UiO) from Norway and P2 -Reykjavik University (RU) from Iceland. Each partner is bringing valuable added value to the project in terms of expertise and available experimental techniques. PP is bringing the expertise in the field of chemical deposition methods, in producing PSCs, and in developing low cost deposition printing techniques; P1 has a solid expertise in deposition of inorganic oxide thin films and in characterization of functional materials by various techniques; P2 has expertise in DFT and molecular dynamics as well as in modelling transport properties in complex structures; P3 has an extraordinary expertise on data processing using high performance computing; P4 is a SME with experience in manufacturing and commercialization of photovoltaic modules and systems.

The main research activities employed by each partner are shortly described below:

PP-NIMP:

- synthesis, deposition and chemistry optimization of the component layers in PSCs structures; that is including different electron transporter materials (TiO_2 and SnO_2) and compositional engineering of the halide perovskite material.
- advanced chemical, structural and optical analyses (XRD, SEM, Raman, AFM, FTIR)
- development of the printing technnology and of the chemical methods to prepare the precursor materials; solvent engineering needed for passing from small area spin-coating technique to the deposition of the perovskite layer using large area techniques (slot-die) were the use of anti-solvents is not possible anymore. Two different printing methods are used, the spray deposition for the ETL oxide films and slot die for depositing the perovskite and organic layers in PSC structures
- fabrication of small and large area standard and inverted PSCs
- electrical and photovoltaic characterization of small and large areas PSCs, a necessary step to provide experimental quantities necessary as inputs for theoretical modelling (J-V characteristics, EQE, PCE, impedance spectroscopy)
- in addition to the role envisaged in the project, PP addressed also the deposition of Cu and Ni oxides by sputtering.

P1 - UiO:

- Synthesis of oxide films used as HTM in the inverted PSC devices, CuO_x and Cu:NiO;
- Structural and chemical characterization of the Cu and Ni oxides (XRD, FTIR, Hall measurements, resistivity)

P2-RU:
– DFT calculations to describe the band alignment at the new perovskite/ETM interface (e.g. SnO_2 as ETM) and a characterization of the TiO_2/SnO_2 interface

- DFT calculations to describe the band alignment at the interface between the perovskite and the inorganic HTM (e.g. Cu_2O, other transition metal oxides).
- Modelling iodine migration in the HP layer using molecular dynamics. Force field parametrizations from DFT calculations used as input for molecular dynamics codes (LAMMPS).

P3-IFIN-HH:
– modelling of dynamic characteristics of both standard and inverted structures

- Comprehensive study of hysteresis phenomena in perovskite solar cells
- Identification of the most probable degradation mechanism, correlation with the hysteresis behavior and negative capacitance measured at low frequencies
- Development of a measurement protocol for correct determination of PCE and its degradation

P4-WATTROM:

- Contributes with its expertise on encapsulating, modules fabrication and testing procedures
- elaborate encapsulation procedures for small and large area PSCs produced by PP
- perform the encapsulation and design the degradation tests

Research and Results in 2023

Explanation of the work carried out by the participants
Below we describe the work carried out by the participants in 2022 according to the EEA 36 project, workpackages and tasks: **WP1: Preparation of standard PSCs** (PP-NIMP and P1-UiO) ***T 1.5. HTM engineering*** In the framework of this specific task, **PP (NIMP)** continued the research on HTM layers engineering for future designs of PCSs. Attention has been payed to the fabrication (by radio-frequency magnetron sputtering, RF-MS) of compositional series of copper-doped nickel oxide thin films. The deposition system modification (oriented towards translation to large-area), implemented in the previous stage of the project, were put to good use. Thereby, the deposition experiments were carried out in the updated UVN-75R1 RF-MS system, equipped with a RF (1.78 MHz) generator and the new 4-inch in diameter magnetron cathode. Cu-doped NiO layers (**$Ni_{0.95}Cu_{0.05}O$**, **$Ni_{0.90}Cu_{0.10}O$**, **$Ni_{0.85}Cu_{0.15}O$**), as well as **pure NiO** and **Cu_2O films** (used as references) were prepared. Simply-pressed (in a metallic shallow dishes) powder were utilized as cathode targets instead of compacted (sintered variants). Either Cu_2O-NiO powder mixtures (in corresponding stochiometric amounts) or Cu_2O and NiO powders, respectively, were accordingly used. This approach offers several definite advantages: (*i*) it permits the use of higher electrical powers without the risk of irreversibly

damaging or cracking the compact targets; and (*ii*) it facilitates the fabrication of reproducible coatings, as these targets can be easily reassembled before each deposition session, ensuring a fresh target surface each time.

The films were deposited at RT onto fused silica (Precision Glass & Optics), ITO-covered glass (Precision Glass & Optics), and intrinsic Si <100> (Si-Mat) substrates, subjected to *ex-situ* (ultrasonic degreasing in acetone, followed by wash in iso-propanol, and then in distilled water, for 10 min each, and then dried in argon flow) and *in-situ* (out-gassing and then argon ion etching) cleaning stages.

First, a base pressure of ~4 × 10^{-4} Pa was attained in the deposition chamber. Further, the high purity argon was admitted at a gas flow of 39 sccm, up to a total pressure of 0.3 Pa. Prior to the deposition of films, the target was pre-sputtered in the working conditions for 30 min, to ensure a clean and activated surface. The films were deposited at a target-to-substrate distance of 35 mm. Films with thicknesses of ~100 nm were prepared based on the deposition rates determined previously by spectroscopic ellipsometry measurements.

First, the chemical structure of the films deposited onto the IR transparent double-polished <100> Si substrates was explored by Fourier-transform infrared (FTIR) spectroscopy in transmission mode, under vacuum. A Jasco 6800-FV-BB spectrometer (Jasco Corporation, Tokyo, Japan), with the spectra being acquired in the wave numbers range of 800–100 cm^{-1}, at a resolution of 4 cm^{-1}. Collecting the IR absorption spectra under vacuum allowed access deep into the far-IR region, where most metallic oxides manifest their bonding vibration modes.

The comparative FTIR spectra of the pure NiO and Cu_2O and Cu-doped NiO films are presented in Fig. 1. The pure Cu_2O film exhibited the high-intensity habitual vibration band centred at ~612 cm^{-1}. To the difference, the NiO-based films elicited their most prominent vibrational band at ~388 cm^{-1}, with a shoulder at ~596 cm^{-1}. The incorporation of Cu in the NiO films resulted in a gradual broadening of spectral envelopes, accompanied by a blue-shift of the maxima. The observed vibrational behaviours are indicating that Cu doping of the NiO films occurs, resulting in a decrease of the structural order, whose structure was probed by FTIR spectroscopy and XRD analyses (Fig. 1–a,b). It was showed that by incremental Cu doping into NiO films it is possible to engineer their electrical properties (as showed by resistivity measurements, Table 1).

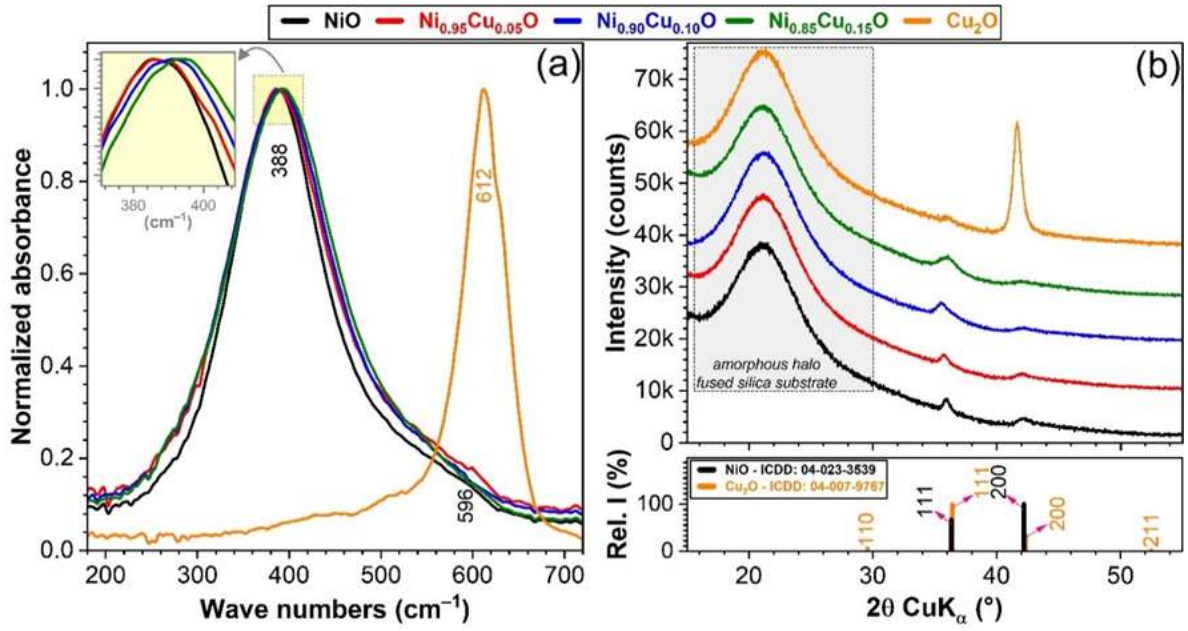

Figure 1: *Comparative (a) FTIR spectra and (b) XRD patterns of the sputtered pure (NiO and Cu_2O) and Cu-doped NiO films prepared by PP-NIMP.*

Table 1: *Electrical properties of the sputtered NiO and Cu_2O and Cu-doped NiO films.*

Sample code	*Resistivity (Ω cm)*	*Carrier concentration (cm^{-3})*
NiO	*1.4*	*1.9×10^{15}*
$Ni_{0.95}Cu_{0.05}O$	*0.5*	*5.7×10^{18}*
$Ni_{0.90}Cu_{0.10}O$	*0.5*	*2.2×10^{19}*
$Ni_{0.85}Cu_{0.15}O$	*0.45*	*2.0×10^{18}*
Cu_2O	*0.55*	*1.9×10^{18}*

In Table 2 are given the NiO Carrier Selective Contact for solar developed by **P1-UiO**. These samples were deposited by sputtering in different conditions, optically and electrically characterized (transmittance, absorption, binding energy, I-V characteristics).

Sample	Sub. Temp. (°C)	NiO/NiO:Cu	Power (w)	Thick. (nm)
NiO:Cu-S6	150	NiO/NiO:Cu	70/70	13
NiO:Cu-S8	150	NiO/NiO:Cu	50/70	18
NiO:Cu-S14	150	NiO/NiO:Cu	40/70	13
NiO:Cu-S13	150	NiO/NiO:Cu	30/70	15
NiO:Cu-S16	150	NiO/NiO:Cu	20/70	13
NiO:Cu-S1	RT	NiO:Cu	70	13
NiO	RT	NiO	70	13

Table 2: *Samples prepared by* ***P1-UiO*** *(sputtering).*

T 1.6. Fabrication of small and large area standard PSCs

In 2023 we have continued the study of the optimization of the fabrication of small (0.083 cm^2) and large-area (2.4 and 4.48 cm^2) standard PSCs using slot-die method, avoiding the use of anti-solvents Some examples are given in Fig.2.

We have developed a simple slot-die coating technique for lead halide perovskites on heated substrates with temperatures of about 90 °C under ambient conditions. By using the best conditions obtained in the previous studies, precursor solution concentration – 1.4 M, distance - 2000 µm, speed - 5 mm/s, pump flow rate - 400 µl/min, during this period our attempts had focused on:

a) Utilization of a hot air flow for drying step
b) Influence of the temperature on the top of the table of dr. Blade apparatus
c) Introduction of a vacuum treatment after the deposition of the perovskite layer
d) Storing in air instead of inert atmosphere
e) TiO2 deposition by slot die
f) The electrodes area – large area
g) Reproducibility
h) Stability/ Degradation
i) Number of pulverization- thickness of TiO_2 compact and mesoporous

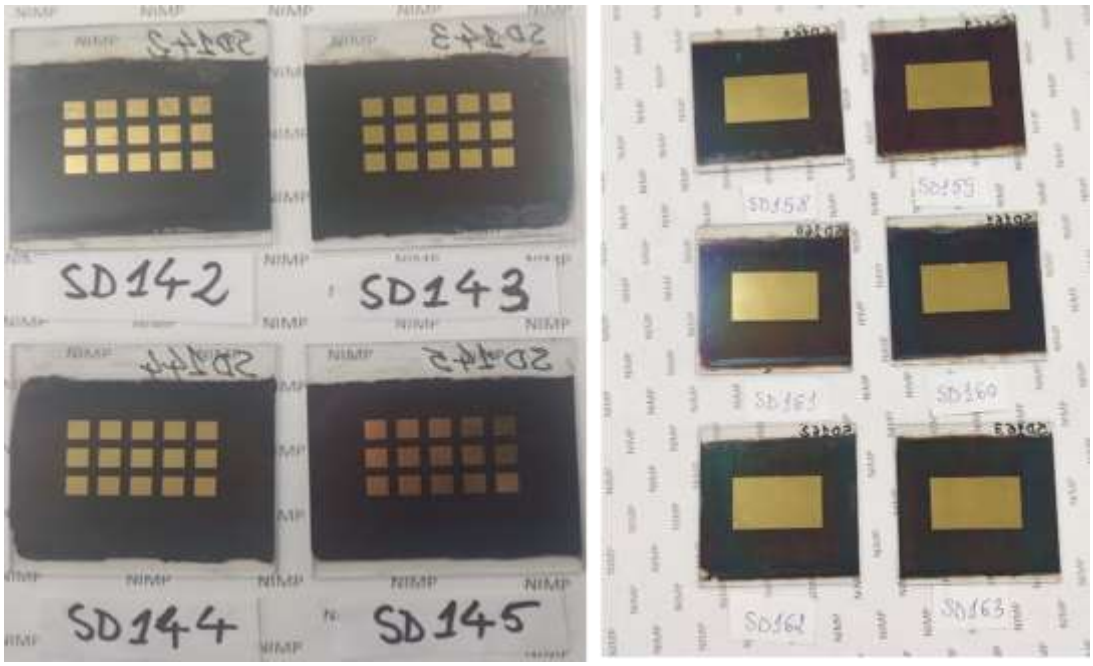

***Figure 2**. Small and large area PSCs deposited by slot-die printing technique.*

Additionally, in parallel we performed studies for developing environmentally friendly perovskite solar cells, by partially replacing Pb with non-toxic elements, such as alkaline earth metal ions (Mg2+) and transition metal ions (Zn2+). Zn was found more suited to partially replace Pb in order to obtain films with higher quality. The resulting solar devices have shown a slight enhancement of the photovoltaic performances and better reproducibility compared to the pristine $MAPbI_{2.6}Cl_{0.4}$ based solar cells.

The information found during this study could be of significant importance in the field of applied materials also from technological point of view, and could lead to advances in the field of PSCs, device development and manufacturing.

WP2: Preparation of inverted PSCs (PP-NIMP and P1-UiO)

T 2.4. Production of small and large area inverted PSCs

The experiments of slot-die large area deposition performed in 2022 were continued for some months in 2023, including testing of other compositions for the perovskite active layer. Although all these perovskite compositions gave good results when deposited in standard PSCs, they did not provided encouraging results in inverted PSCs, the performance and reproducibility of the fabricated inverted PSCs being very poor compared with standard PSCs. We found that the main reasons behind are:

1. Inverted PSCs contain, beside the perovskite absorber, other different films of organic materials (PEDOT; PSS, $PC_{60}BM$, BCP), each of these materials having slightly different properties for each purchased batch, mostly due to the different quantities of by-products still present after their synthesis. In addition, these materials are expensive and their scaling to a large area not only increases the costs considerably, but the properties of each film require many intermediate optimization steps;
2. On the small area the efficiency of these devices was low, little over 6% for the devices with ITO/ PEDOT:PSS/ FAMA10K / PCBM 4 mg/ml/ BCP/ Au, less than half of the efficiency obtained with solar cells with standard geometry. Moreover, this efficiency was obtained when the additional film of BCP was introduced, deposited by thermal evaporation in vacuum, which can not be scaled to a large area as envisaged by the project scope;

3. Passing to large area deposition by slot-die technique and skipping the very toxic anti-solvent treatment, the performance of inverted PSCs dropped even further;

Therefore, in April 2023 we gave up on the development of inverted solar cells at large scale, in agreement with the Yes/NO decision foreseen in month 27 in WP5.

WP 3: Modelling of materials and interfaces (P2-RU and P3-NIPNE)

The theoretical work in 2023 was jointly performed by **P2(RU**) and **P3(NIPNE)** on:

T 3.4 Ab initio DFT calculations for band alignments

Ab initio DFT calculations for band alignments between the halide perovskite (HP) layer and electron transporter layers and numerical analysis of bias stress test in order to anticipate the PSC degradation have been performed. It has been determined that replacement of of MA^+ by FA^+ ions can enhance crystallinity, absorption, and carrier lifetime of the lead halide perovskite. *Ab initio* DFT analysis has been performed to analyze bulk $MAPbI_3$, $FA_{0.5}MA_{0.5}PbI_3$, and $FAPbI_3$ perovskite materials. The structures under investigation are being assembled by tetragonal tin oxide SnO_2 and compositional $FA_xMA_{1-x}Pb(I_yCl_{1-y})_3$ perovskite obtained by doping FA^+ and Cl^- ions into parental methylammonium lead triiodite perovskite $MAPbI_3$. The *ab initio* density functional theory (DFT) calculations are implemented using the SIESTA package, which represents a suitable computational framework for relatively large systems. SIESTA package operates using numerical atomic orbitals as basis set. The results are detailed in D14 and summarized in the next section.

WP4: Device characterization and modelling (PP-NIMP-P2-RU and P3-NIPNE)

PP (NIMP), P3 (NIPNE) and **P2(RU)** have jointly worked in this workpackage:

T 4.3 Numerical analysis of bias stress tests**,** by characterizing and modelling the hysteretic behaviour of PSCs under different conditions: 1) Impact of the bias poling (V_{pol}); 2) Impact of the scan rate (α); 3) Impact of the bias range (V_0).

Three types of fabricated PSCs, including FAMA as the perovskite absorber have been studied: (a) ITO/c-TiO_2/m-TiO_2/FAMA; (b) ITO/c-TiO_2/m-SnO_2/FAMA; (c) ITO/c-TiO_2/QD-SnO_2/FAMA. In these structures only the mesoporous layer is different in composition (TiO_2 vs. SnO_2) or morphology (mesoporous, m-SnO_2 vs. quantum dot layer, QD-SnO_2). The experimental and modelling results are given in the second part of this report.

WP5: Device encapsulation and modules production and testing in standard operation conditions (PP-NIMP and P4-WATTROM)

Both **PP(NIMP)** and **P4 (WATTROM)** had jointly worked on:

T 5.1 Encapsulation of the individual small and large area PSCs

The encapsulation of large area cells (4 of 2.4 cm^2 on 5 cm x 5 cm glass/FTO substrates) was performed with EVA (ethylene-vinyl acetate copolymer) and PET (Polyethylene terephthalate Solar Backsheet) foils which are commercially used in the case of Si-based photovoltaic panels. The tests with EVA foil incapsulation of *fresh* standard PSCs fabricated with slot-die printing technique and without the toxic processing step of “solvent extraction” revealed that this healthy approach has an important drawback- the solvent used to prepare the “ink” remains partly in the deposited perovskite layers and continue dissolving the perovskite layer promoting actually the degradation of the cells. Our test have shown that this fast degradation can be avoided if the fresh PSCs are not immediately encapsulated, but kept for at least a month in ambient laboratory atmosphere.

The minimum bonding temperature optimized for perovskite cells is 60 °C (for silicon-based panels is made at 200 °). The employed encapsulation process steps (Fig. 3) are:

1. The solar cell was covered with EVA foil. In order to assure the EVA bonding on the solar cell surface, the cell was placed for 5 minutes on a hot-plate fixed at 60 °C;

2. The PET foil was added on top of EVA foil, while keeping the solar cell on the hot plate (60 °C). The PET foil was lightly pressed with a glass slide for 5 minutes at 60 °C;
3. The solar cell was removed from the hot-plate and to cool down to room temperature.

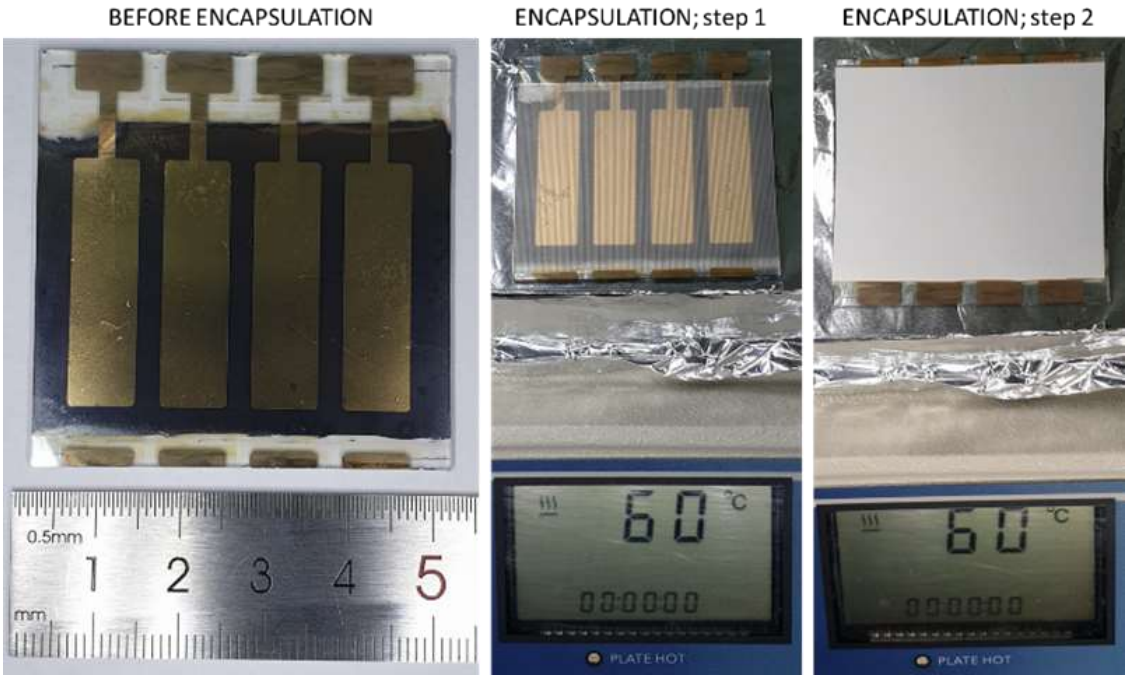

Figure 3: *Encapsulation process of photovoltaic modules (5cmx5cm) of PSCs.*

The encapsulated solar cells were tested under various humidity conditions (from 40 % to 90%), while the open-circuit voltage (V_{oc}) was recorded simultaneously with an oscilloscope. The open circuit voltage is constant irrespective of the relative humidity, from 44% up to 86% (Fig. 4), showing that the performance of standard PSCs and small photovoltaic modules is preserved after encapsulation even in high humidity conditions.

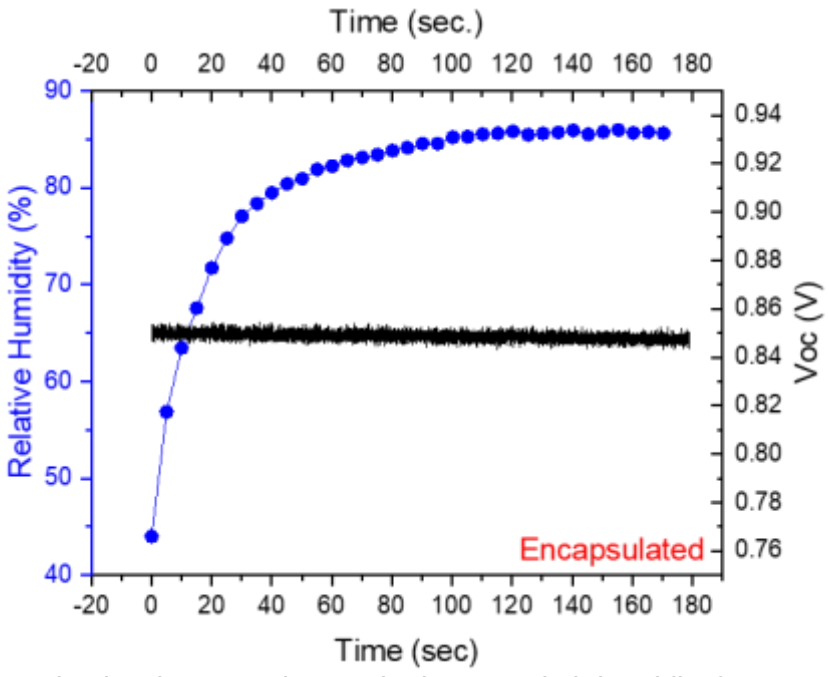

Figure 4. *Open circuit voltage vs. time under increased air humidity for encapsulated cell.*

T 5.2 Manufacturing of small photovoltaic modules and their testing

Small photovoltaic modules (5 cm x 5 cm), each with 4 large area PSCs (see Fig.3), have been fabricated and tested before and after encapsulation (see **T.5.1.** above)

T 5.3 Manufacturing of PV panels, their testing and cost assessment

Phtovoltaic modules of 15x15 cm^2 with a stabilized PCE between 3 and 6% were produced by connecting 9 large area PSCs, each of them of 4.48 cm^2 printed on 5 cm x 5 cm FTO covered glass substrates. These PV modules can power different devices, e.g. the windmill in Figure 5.

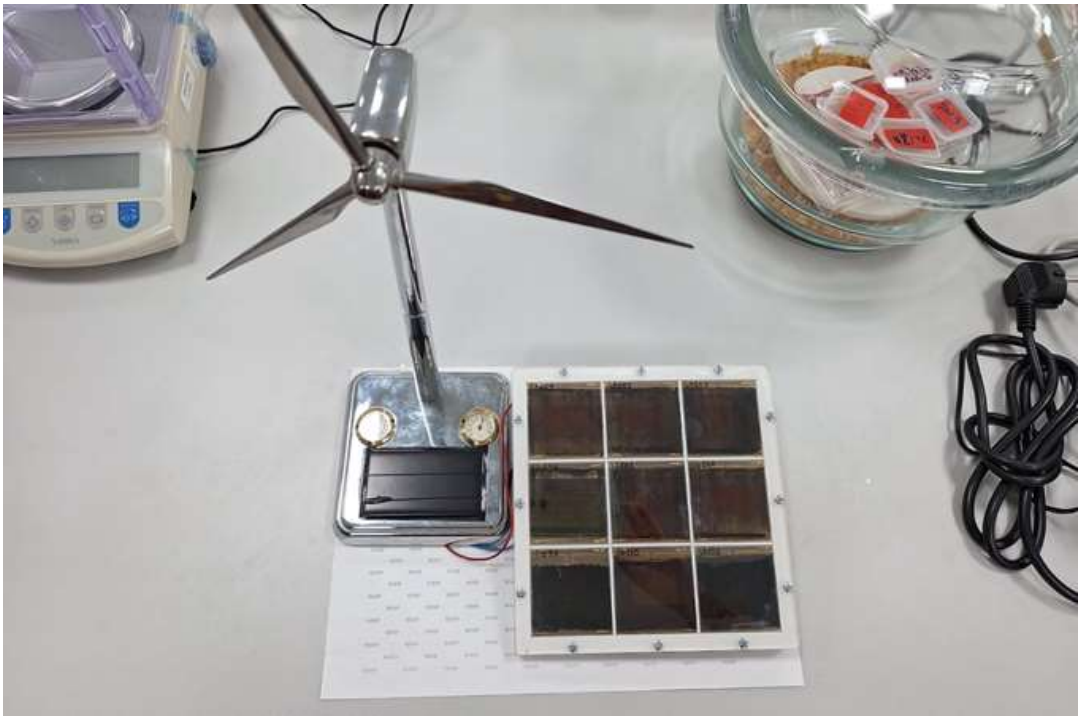

Figure 5. *PV module of 15x15 cm^2. The active area of the device is 40.32 cm^2.*

For a 5 x 5 cm^2 sample with an active area of 4.48 cm^2 the breakdown of fabrication costs in laboratory conditions (without labour costs) is:

- glass/FTO substrate: 90 RON
- Compact TiO_2 uses 0.25 mL Ti^{4+} precursor and 7.5 mL anhydrous IPA: 3.92 RON
- Mesoporous TiO_2 uses 0.0375 g TiO_2 paste and 7.5 mL anhydrous EtOH: 2.34 RON
- Perovskite layer uses 0.2 g DMF, 0.026 g DMSO, 0.1229 g PbI_2, 0.0185 g $PbCl_2$ and 0.053 g MAI: 1.18 RON
- HTM layer uses 4 mg Spiro-oMeTAD, 0.468 mg Li-TSFI, 50 µL CB, 0.9 µL ACN and 1.4 µL pyridine: 6.97 RON
- Au electrode of 100 nm and an area of 4.48 cm^2 contains approx. 0.9 mg material, with an average price in the last 6 months of 292 RON/g leads to a cost of :0.26 RON

The consumption of energy (electricity) for the involved thermal treatments (1h at 500 C for TiO_2 and t below 100 C for the other layers) is estimated at 0.9 kWh. By far the most expensive component is the cost of glass/FTO substrate we bought for our research.

WP6: Management, reporting, dissemination and patenting

All the partners participate in managing their resources and disseminate the results. PP(NIMP) took care of the project management, project webpage and made the yearly report based on the specific contributions of the partners.

Overview of the progress of work towards the objectives of the project, including milestones (M) and deliverables (D) identified in the project contract for year 2023.

The progress of the work performed in 2023 towards the project objectives is shortly described in the following, with respect of the deliverables (D) and milestones (MS) foreseen for the year 2023:

- **D12. Report on the replacement of organic HTM with inorganic oxides in standard PSCs – (P1-UiO)**

The work on inorganic oxides for standard PSCs was took over in 2023 by PP. In order to replace the standard HTM (Spiro-OMeTAD) with inorganic oxides several recipes of depositing Ni and Cu oxides were considered. The main problem is to deposit these oxides at temperatures below 130 C (for preserving the perovskite on top of which are deposited) while obtaining the right electrical properties for transporting holes. Some encouraging results were obtained only for CuO_x when the HP was deposited by spin-coating with the anti-solvent treatment. In the absence of any anti-solvent treatment, the solvent remaining in the printed HP destroys the CuO_x layer. Especially studies concerning the elimination of solvents remaining in the perovskite and Hall measurements are important issues to be further addressed in 2024.

- **D13. Report on the performances of small and large area inverted PSCs – (PP)**

For inverted PSCs we are far from achieving the MS4 milestone, the maximum achieved PCE being obtained on ITO/ PEDOT:PSS/ HP/ **PCBM** / Au structures, of 5.18% and 4.81% on small area PSCs with $FA_{0.7}K_{0.1}MA_{0.2}PbI_{2.8}Cl_{0.2}$ and $MAPbI_{1.8}Br_{1.2}$, respectively. On large area PSCs the obtained PCEs were below 0.5%. For fabricated ITO/PEDOT:PSS/ HP/ **CuO_x:Ni** / Au inverted structures the PCE was below 0.5% even for small area PSCs. For samples with PCBM as ETL we focused on three types of HPs: $MAPbI_{2.6}Cl_{0.4}$, $FA_{0.7}K_{0.1}MA_{0.2}PbI_{2.8}Cl_{0.2}$ and $MAPbI_{1.8}Br_{1.2}$. These compositions were tested as photoactive layers in *inverted PSCs* using PEDOT:PSS as p-type layer and PCBM with or without BCP as n-type. The best performances were obtained on small area devices (0.083 cm^2), as given in Table 3.

Table 3. Solar cells photovoltaic parameters for MAPICl and FAMA10K perovskites, and PCBM with different thickness.

Sample	Structure	PCE max, %	Observations
T 37	ITO/ PEDOT:PSS/ FAMA10K/ Au	3.24	Large hysteresis
T 85, T 86	ITO/ PEDOT:PSS/ FAMA10K/ PCBM 4 mg/ml/ Au	4.3, 4.6	Large hysteresis
T 87	ITO/ PEDOT:PSS/ FAMA10K / PCBM 4 mg/ml/ BCP/ Au	6.155	Large hysteresis
T 88	ITO/ PEDOT:PSS/ FAMA10K/ PCBM 5 mg/ml/ Au	2	Medium hysteresis
T 90	ITO/ PEDOT:PSS/ FAMA10K / PCBM 5 mg/ml/ BCP/ Au	5.47	No hysteresis
T 91, T 92	ITO/ PEDOT:PSS/ FAMA10K/ PCBM 6 mg/ml/ Au	5.09, 4.98	Small hysteresis
T 93	ITO/ PEDOT:PSS/ FAMA10K / PCBM 6 mg/ml/ BCP/ Au	5.38	No hysteresis

These results show that the PCE values are quite close for all samples when different dilutions of PCBM are used. BCP proved to be to some extent helpful; the corresponding

curves are more reproducible and less noisy (fig. 6). However, introducing a time-consuming thermal evaporation step is time consuming and it is requires extensive experiments for optimization. So far, this is the **best result** obtained with inverted solar cells. Additionally, these experiments confirmed that although the 5 mg/ml PCBM solution results in cells with the best efficiency, the reproductibility rate is poor of often appear short-cuts.

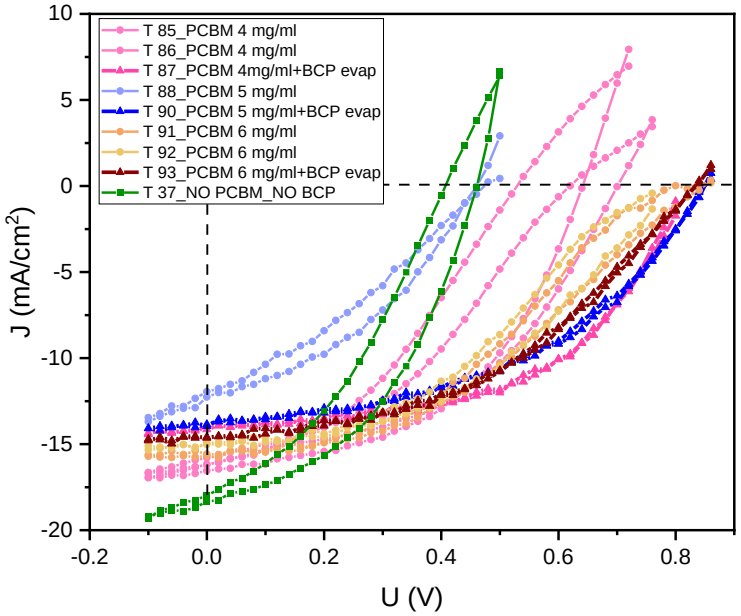

Figure 6. *J-V curves for PSCs with slightly different thickness of the n-type layer*

- **D14. Band alignments in PSC structures – (P2, M36)**

Ab initio density functional theory analysis has been performed to analyze bulk $MAPbI_3$, $FA_{0.5}MA_{0.5}PbI_3$, and $FAPbI_3$ perovskites – see Fig. 7.

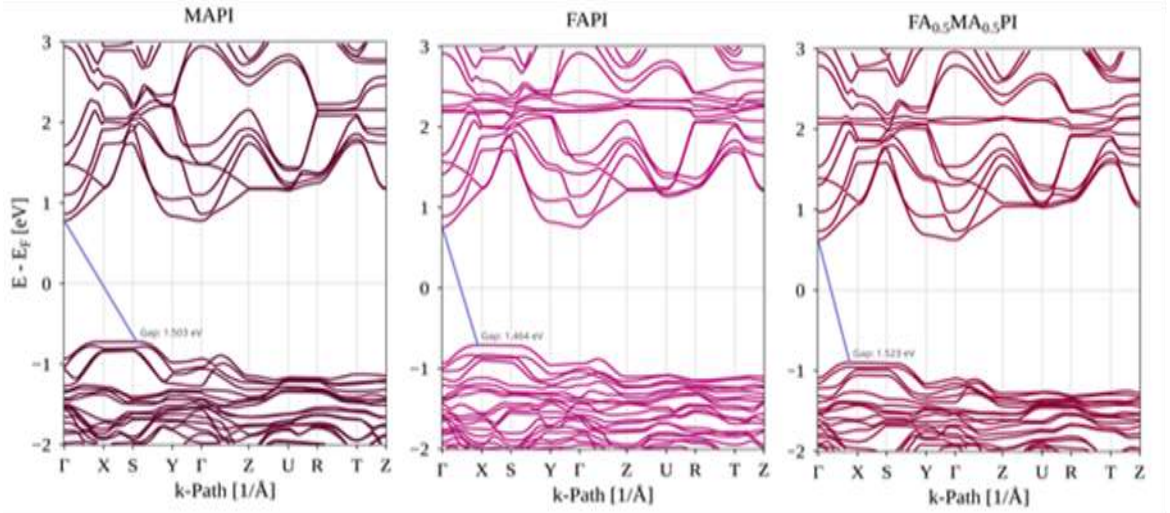

Figure 7: *Band structures for bulk $MAPbI_3$, $FAPbI_3$, $FA_{0.5}MA_{0.5}PbI_3$ using LDA calculations. These are optimized for the FAMA@SnO_2 interface calculations.*

The ideal **$FA_xMA_{1-x}PbI_{3-y}Cl_y$@$SnO_2$ interface** is depicted in Fig. 8 (without doping after relaxation procedure, with Cl and FA^+ doping). The investigated structures have been assembled by tetragonal SnO_2 and compositional $FA_xMA_{1-x}Pb(I_yCl_{1-y})_3$ obtained by doping FA^+ and Cl^- ions into parental $MAPbI_3$.

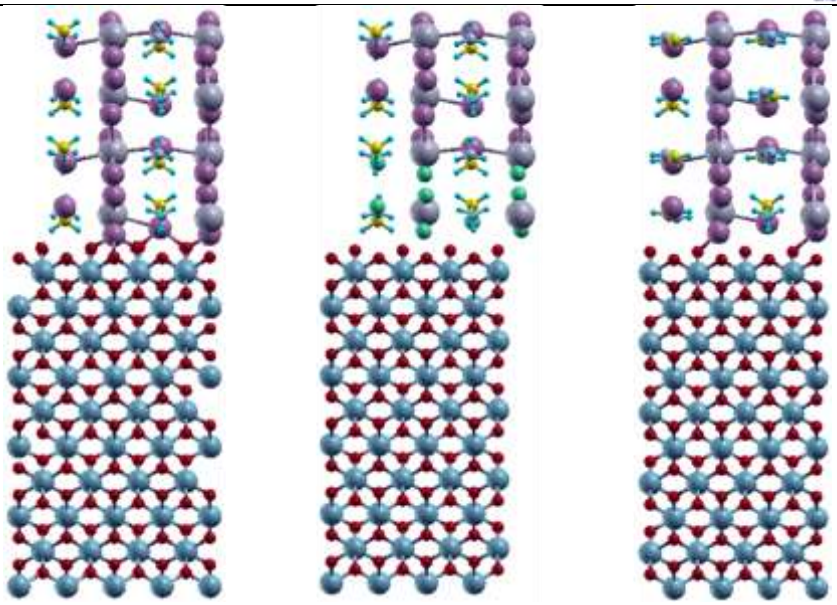

Figure 8: *Atomistic depiction of $MAPbI_3@SnO_2$ interface after relaxation procedure, $MAPbI_yCl_{1-y}@SnO_2$ with 3 layers of Cl^- dopants and $FA_xMA_{1-x}PbI_3@SnO_2$ interface with 25%-75% proportion of MA^+-FA^+ cations. (Left to right).*

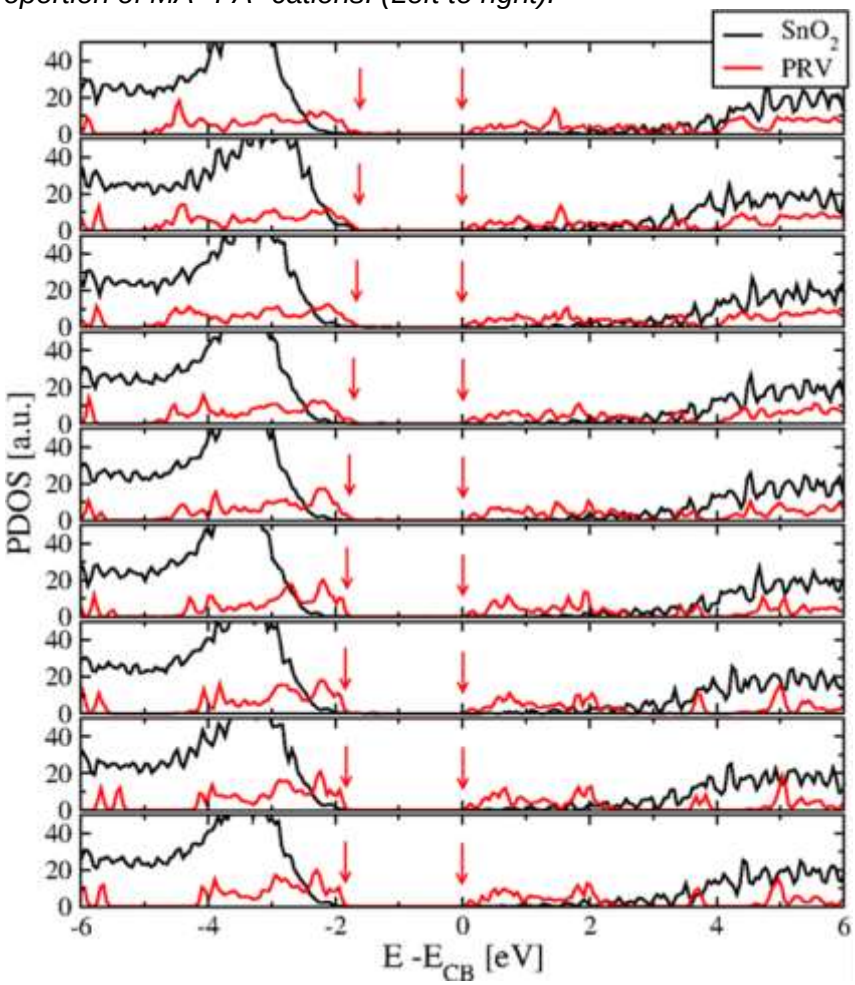

Figure 9: *Density of states analysis of $FA_{0.5}MA_{0.5}PbI_yCl_{y-1}@SnO_2$ interface with increasing concentration of chlorine substituted on iodine top to bottom layer. PDOS for SnO_2 middle layer (atoms nr. 73-176) is shown with black line, for middle layer of $FA_{0.5}MA_{0.5}PbI_yCl_{1-y}$ (atoms nr. 271-306) with red line. The arrows evidence the bandgap*

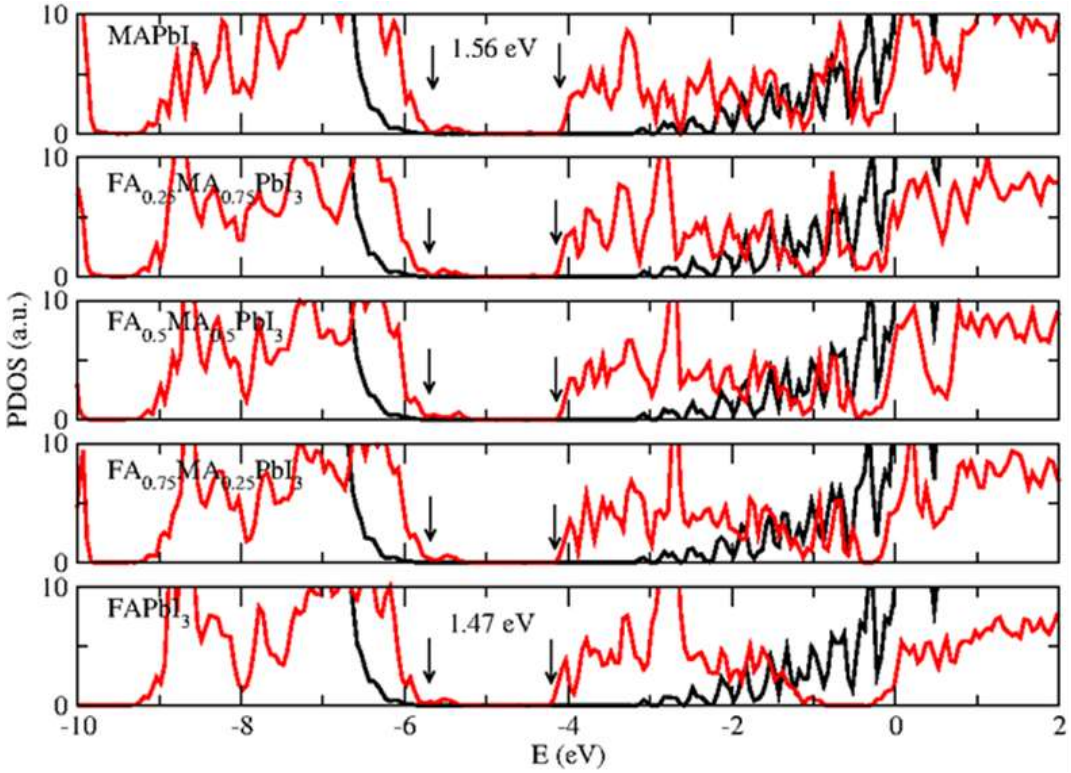

Figure 10: *Density of states analysis of the SnO_2/$FA_xMA_{1-x}PbI_3$ structures. PDOS for SnO_2 middle layer (atoms nr. 73-176) is shown with black line, for middle layer of $FA_xMA_{1-x}PbI_3$ (atoms nr. 271-306) with red line.*

In Fig. 8 is shown $MAPbI_3$ with first three layers of I^- substituted by Cl^- ions. Similarly, the Cl ions are substituted in $FA_{0.5}MA_{0.5}PbI_3$ structure. The Cl on I substitution increases gradually for the 9 structures in Fig. 9.
The structures (1) and (9) correspond to $FA_{0.5}MA_{0.5}PbI_3$ and $FA_{0.5}MA_{0.5}PbCl_3$, respectively. In structures (2)-(8) the Cl concentration is increased gradually layer by layer. According to PDOS of middle layers of SnO_2 and $FA_{0.5}MA_{0.5}PbI_yCl_{y-1}$, all structures (1)-(9) display a bandgap. An increase of the bandgap value with the increase of Cl concentration is observed. This way, Cl doping represents an excellent way to control the bandgap of HPs at the junction.
Fig. 10 shows the change in PDOS with increasing FA^+ ions substitution in $MAPbI_3$. Top figure corresponds to $MAPbI_3$@SnO_2 interface, while the bottom one to $FAPbI_3$@SnO_2 junction. The concentration of FA^+ ions substitution is increased by 25% in each following plot. The bandgap decreases with FA^+ doping, in agreement with the findings presented for band structures of bulk HPs in Fig. 8.

- **D15. Device specific J-V characteristics and simulations – (P3)**

In our recent study, [Phys. Rev. Applied 18, 064087 (2022)], a new Ansatz for the recombination current was introduced, which explains the capacitive and inductive effects.

$$I_{\text{rec}} = I_{\text{rec0}} + aQ_c + bI_c = I_{\text{rec0}} + aQ_c + b\frac{\partial Q_c}{\partial t}$$

where: I_{rec0} – is the base recombination current in the absence of ions; a – reflects the impact of ionic charge accumulation on the recombinations; b – reflects the recombination due to internal electric fields (proportional to the ionic currents). We investigated the impact of these parameters under repeated bias sweeps. Studying the modifications in J-V

characteristics in a relatively short time-span after fabrication can provide information concerning the future degradation of PSCs. Two main investigation tools are the J-V hysteretic effects and impedance spectroscopy. The former is more flexible and easier to implement. We therefore focus on J(V) dependence, during repeated bias scans, and account for the variations of I_{rec0}, a, b parameters.

Figure 11(a) shows 10 J-V scans considering a linear increase in I_{rec0}, from 1 mA to 1.5 mA. This corresponds to an increase in the base recombination current with increasing the number of sweeps. The basic effect is a reduction of the short-circuit, as well as of the collected current. The current bump, which appears in the first scan, is not anymore present for the subsequent scans, as the induced initial polarization reflected in ionic accumulations decays in time. Adding the contribution due to ionic recombinations, by linearly varying a in the interval (0,100) s^{-1}, we obtain the J-V sequence in Fig. 11(b). Here, in addition to reducing the short-circuit current, an effective decrease of the shunt resistance is observed. However, this is due to the increased rate of recombination as the ionic induced defects become more effective for electron-hole recombinations.

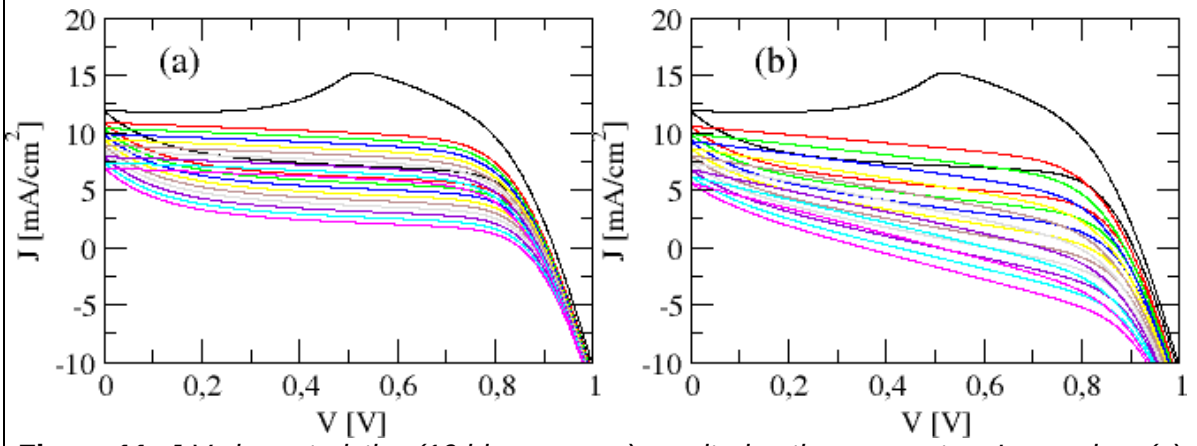

Figure 11: *J-V characteristics (10 bias sweeps) monitoring the parameters I_{rec0} and a : (a) a=0 and linear increase of I_{rec0} → decrease of the short circuit current; (b) Linear increase in both I_{rec0} and a → in addition, an effective reduction of the shunt resistance is observed.*

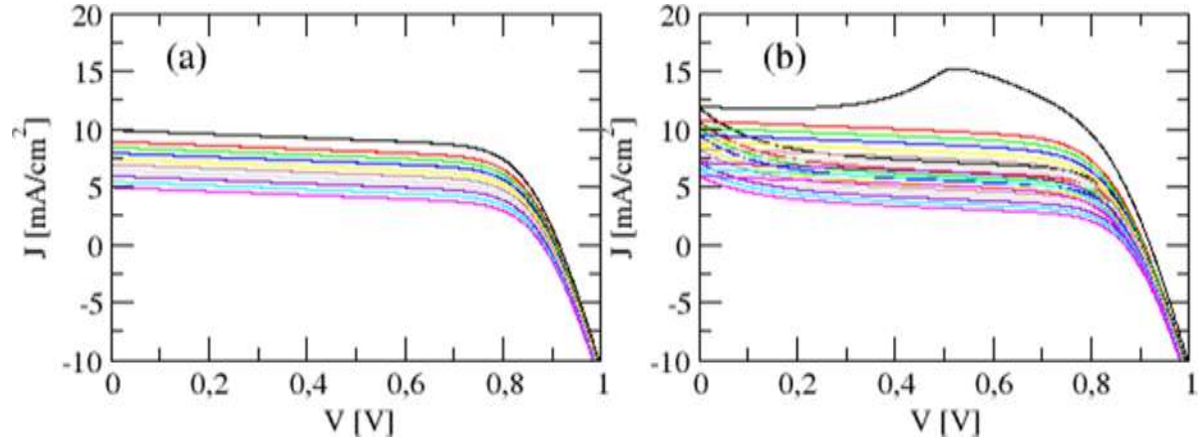

Figure 12: *J-V characteristics (10 bias sweeps) monitoring the parameters I_{rec0} and b: (a) b=0 and linear increase of I_{rec0} → no hysteresis and reduced short-circuit current; (b) Linear increase in I_{rec0}, while b is reduced → hysteresis becomes smaller with increasing the umber of bias sweeps, as the sample stabilizes.*

Figure 12(a) shows stationary J-V characteristics, assuming the capacitive effects are small (or equivalently, the bias scan rate is small). The same trend is observed in the short-circuit

current, increasing $I_{rec0,}$ however, without dynamic hysteresis. Introducing a linear variation for the *b* parameter from 1000 to 500, we obtain a decrease in the hysteresis magnitude, as it can be observed in Fig. 12(b). This corresponds to a stabilization of ion migration in the sample. Conversely, if the *b* parameter is increased, larger hysteresis is expected as the repeated bias scans are performed. This would correspond to an enhanced migration of the ionic species during the bias stress tests. Ultimately, the relevant trend will be identified from the experimental data. These behaviors can be identified in different prototype PSCs and can aid in the classification of the dominant processes related to ion migration: (i) the magnitude of ion migration by examining the hysteresis magnitude; (ii) potential degradation due to induced defects in the perovskite layer; (iii) accumulations of ions at the interfaces and induced recombinations (parameter *a*); (iv) internal electric field during operation and induced recombinations (parameter *b*). We correlated these observations with experimental data measures on PSCs, depicted in Fig. 13

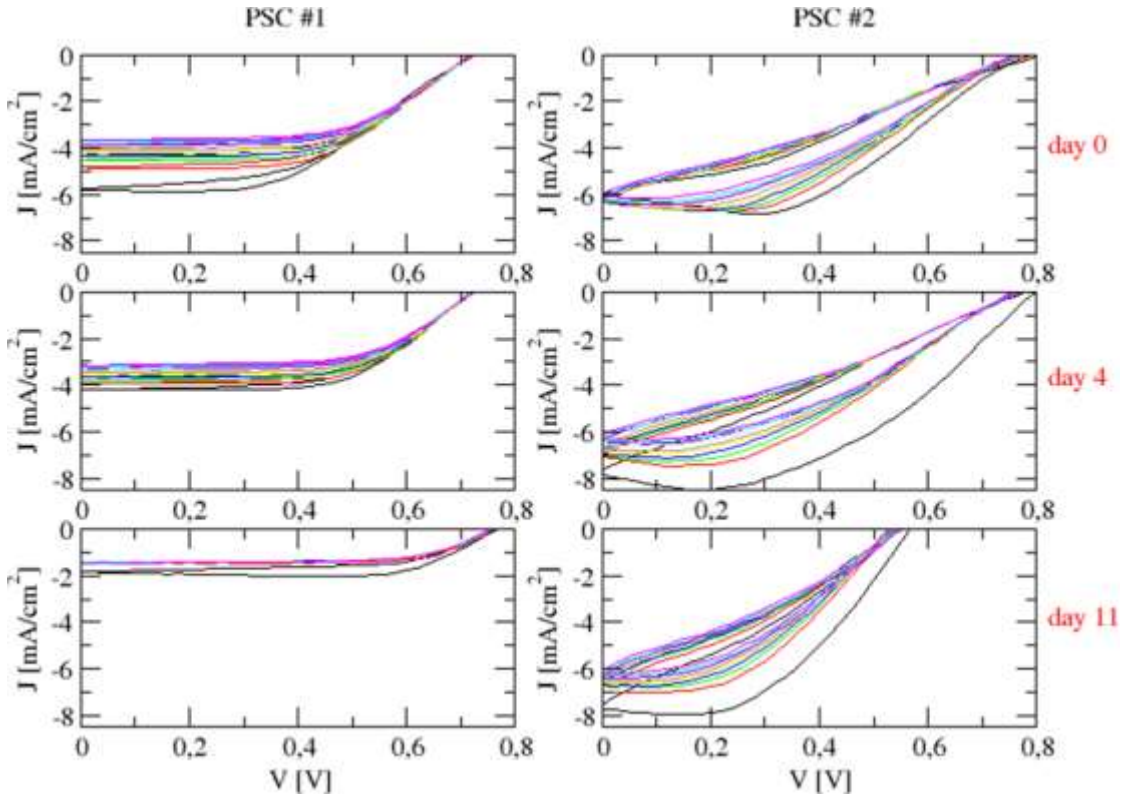

Figure 13: *Two PSCs, labeled with PSC1 and PSC2, exhibit different behavior in the dynamic J-V characteristics and evolutions in time.*

We performed repeated bias scans on two samples, denoted by PSC1 and PSC2, and we monitored their degradation in time, by measuring the dynamic scans as fabricated (day-0) and after 4 and 11 days. PSC1 shows relatively small hysteresis and also a lower PCE. It degrades more quickly than PSC2 and this becomes visible by analyzing just the firs two measurement sets (day-0 and day-4). There one can find a larger spread in the short circuit currents during the 10 sweeps. The first scan has typically a larger hysteresis as theoretically predicted. In the case of PSC2, a larger hysteresis is observed from the very beginning. However, it remains rather stable with increasing the number of sweeps and after repeating the process in day-4. This trend is further confirmed in day-11.

Combining all three contributions a set of J-V characteristics which contain the main features can be obtained. In Fig. 14 we considered an increase in I_{rec0} from 1 mA to 1.5 mA, along with an increase in *a* parameter from 0 to 100 s^{-1} and a decrease of *b* parameter from 1000 to 800.

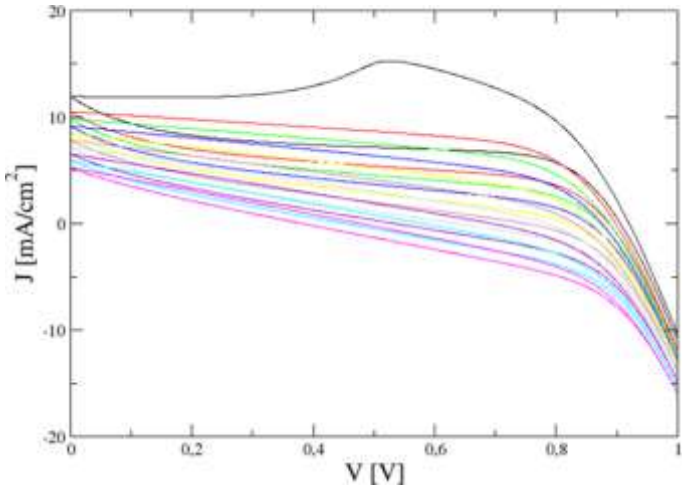

Figure 14: *Dynamic J-V characteristics obtained by varying I_{rec0}, a, and b. A typical behavior emerges (e.g. compare with PSC2): larger hysteresis in the first sweeps, which is gradually decreasing. The short-circuit current is reduced and an apparent shunt resistance lowering can be observed.*

The proposed model was applied for simulating J-V response of three types of PSCs developed by PP, all including FAMA as the perovskite absorber: (a) ITO/c-TiO_2/m-TiO_2/FAMA; (b) ITO/c-TiO_2/m-SnO_2/FAMA; (c) ITO/c-TiO_2/QD-SnO_2/FAMA. In these structures only the mesoporous layer is different (TiO_2 vs. SnO_2) or morphology (mesoporous, m-SnO_2 vs. quantum dot layer, QD-SnO_2). The measured J-V characteristics are shown in Figure 15.

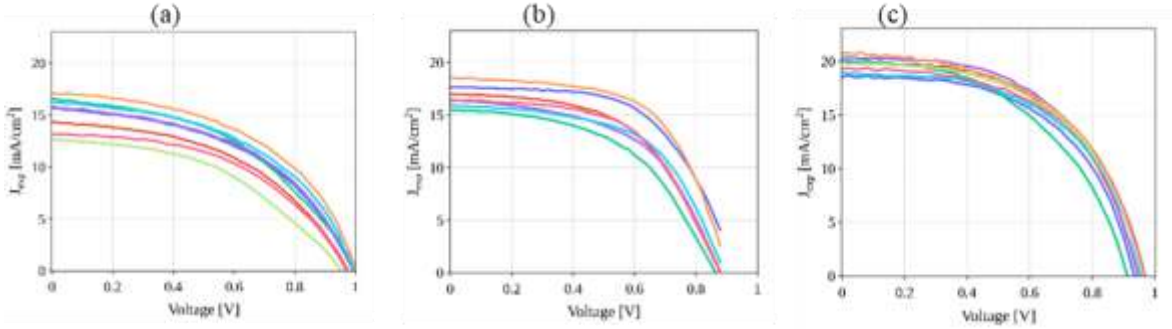

Figure 15: *Experimental (averaged) J-V characteristics for three compositions / morphologies of the active layer: (a) $mTiO_2$; (b)$mSnO_2$; (c) QD-SnO_2. Averages between reverse and forward scans are presented for several contacts on the same probe.*

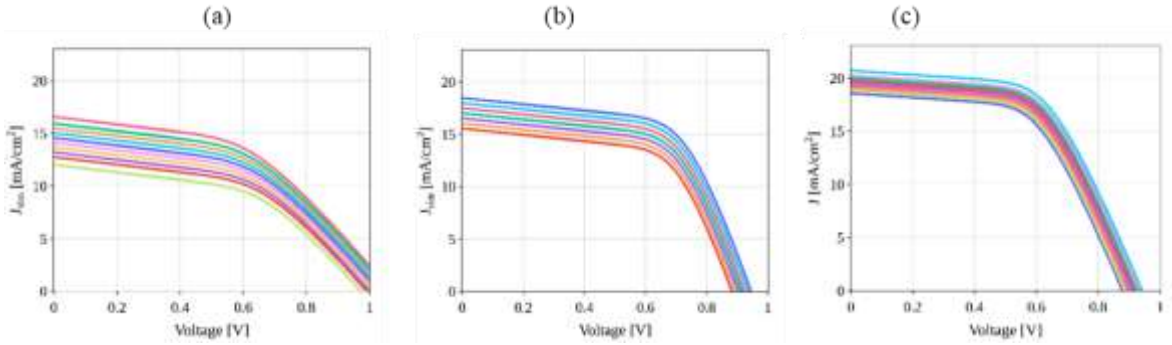

Figure 16: *Simulations of the stationary J-V characteristics in correspondence with the samples indicated in Fig. 11.*

The J-V curves are parametrized to reproduce the general experimental trends. In each set, $J_{rec0,}$ and V_{th}, are varied. For each device type, we found different R_s, R_{sh} pairs for the series and shunt resistances. The parameters leading to the simulations in Fig. 16 are given in Table 4.

Table 4.

	$R_s(\Omega)$	$R_{sh}(k\Omega)$	Min J_{rec0} (mA)	Max J_{rec0} (mA)	Min V_{th}	Max V_{th}
PSC1 (m-TiO_2)	255	2.58	0.18	0.68	0.42	0.46
PSC2 (m-SnO_2)	100	3.30	0.10	0.40	0.38	0.40
PSC3 (QD-SnO_2)	125	5.10	<0.01	0.10	0.37	0.39

The hysteretic effects pose a great challenge for a correct assessment of solar cells PCE. The dynamical model allows to anticipate these effects and acquire the stationary value as close as possible. The most prominent effects, which can alter the PCE determination, are: 1). *Impact of the bias poling (V_{pol})* – Fig. 17. Applying a poling voltage induces an ions accumulation at the ETL/PRV and HTL/PRV interfaces. This is initially compensated by opposite charges on the two electrodes, resulting in a negligible electric field inside HP. However, as the R scan is performed, starting from V_{oc}, the ions cannot follow the rapid voltage change and an electric field appears, enhancing initially the charge collection (e.g. observed as the current bump) and then diminish it as the ions return to the HP bulk (see Fig. 17). The hysteresis becomes more pronounced as V_{pol} is increased.

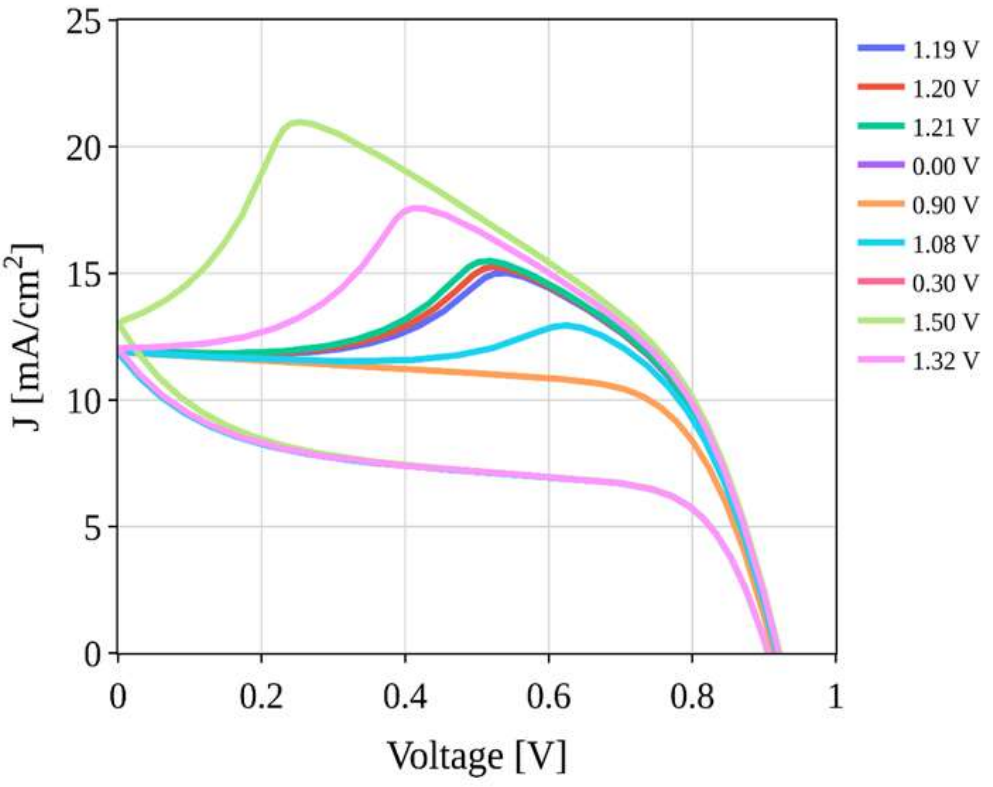

Figure 17: *Dynamic J-V characteristics obtained by increasing V_{pol}.*

2). *Impact of the scan rate (α)*-Fig. 18. By varying α, the hysteresis shape and magnitude are modified. Starting with a relatively small α, of 10 mV/s, the J-V characteristics is closer to the stationary case and the hysteresis is rather small, while the current bump is found near V_{oc}. Increasing α, the hysteresis enlarges, as the ions cannot follow the rapid sweeps. At the same time, the current bump is driven towards smaller voltages (scan time is shorter than the relaxation time) and the short-circuit current I_{sc} is enhanced.

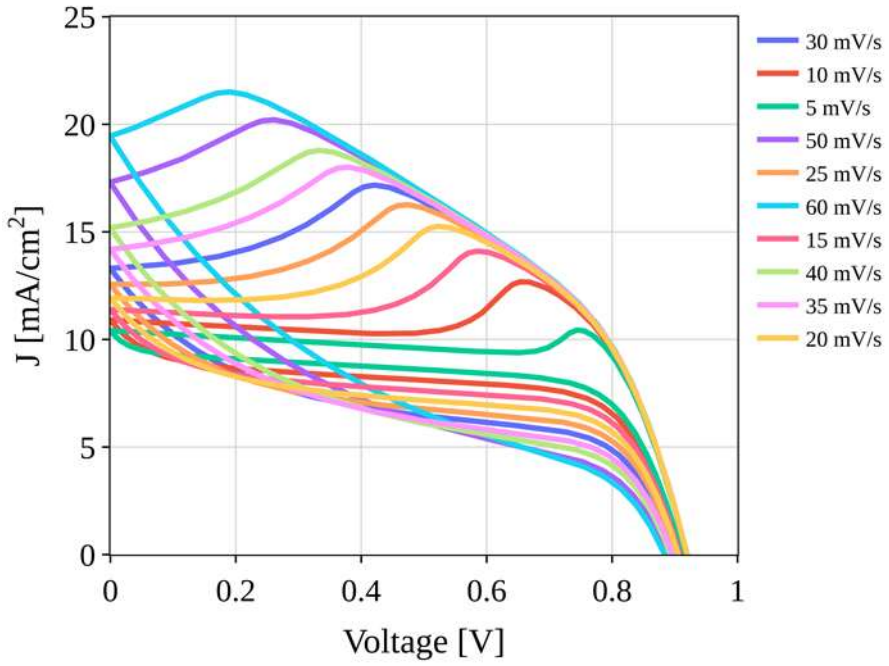

Figure 18: *Dynamic J-V characteristics obtained by increasing the scan rate* α.

3). *Impact of the bias range (V_0)*- Fig. 19. The starting bias in the R scan evidences the decay of the initial (ionic) polarization of the PSC. Reducing V_0, the collected current is initially larger and then decays.

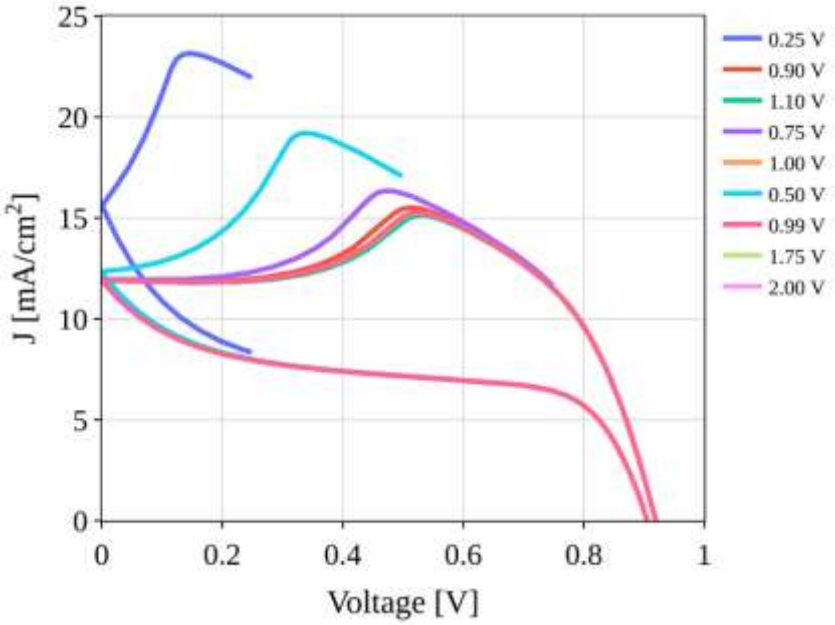

Figure 19: *Dynamic J-V characteristics obtained by decreasing the initial voltage V_0.*

These dynamic behaviors can be identified in different PSCs and can aid in the classification of dominant processes related to ion migration: (i) ion migration by examining the hysteresis magnitude; (ii) potential degradation due to induced defects in the HP layer; (iii) ions accumulation at the interfaces and induced recombinations (parameter a); (iv) internal electric field during operation and induced recombination (parameter b). One important feature influencing the intrinsic degradation is ion migration in the HP layer. It is believed that migration of iodide ions (I^-) is dominated by the diffusion of iodide vacancies (IVAC). By molecular dynamics simulations we found that the addition of a small amount of OH^- ions can help in suppressing the I^- migration and increases the overall stability of HP. Thus, the OH^- can bind to the positively charged IVAC and block the access of I^- into those vacancies. We show that when IVAC are formed, other I atom migrates to fill the vacancy, creating a new vacancy in its place. This process continues throughout the simulation domain until the vacancy reaches boundary lines. In the presence of OH group, the initial I atoms migration will still occur, but, once the newly created vacancy is within one unit cell from the OH group, this group migrates toward the vacancy and remains very close to it.

This work is relevant for **MS5** (Comprehensive models of charge transport and degradation of PSCs). With our molecular dynamics simulations, performed with the LAMMPS software, we found that the addition of a small amount of OH^- ions can help suppress the migration of iodide and increase the overall stability of the material. We showed that the OH^- ions can bind to the positively charged iodide vacancies and can block the access of the negative iodide ions into those vacancies.

We computed with LAMMPS the mean square displacement (MSD) of all iodide ions included in the simulation cell, as a function of the time t,

$$\mathrm{MSD}(t) = \frac{1}{N}\sum_{i=1}^{N} |\mathbf{r}_i(t) - \mathbf{r}_i(0)|^2 \ ,$$

with N being the total number of iodides and $\mathbf{r}_i$ the position of the particular ion i as function of time. The diffusion coefficient associated with the mobile ions can be obtained as

$$D = \frac{1}{6}\lim_{t\to\infty} \frac{\mathrm{MSD}(t)}{t} \ ,$$

which in practice is calculated using the slope of the MSD vs. time, divided by the double of the spatial dimension.

The numerical results of the MSD are shown in Figure 20.

We first consider a simulation cell that in the initial state includes the reference case of an iodide vacancy (IVAC) and no hydroxyl, at room temperature and normal pressure. The corresponding MSD is shown in blue, and the slope is as expected from previous studies. Then, in Test 1 we repeat the simulation by adding an OH^- group in the same unit cell as the IVAC. Further, in Tests 2, 3, and 4, we increase the initial distance between the IVAC and the OH^- group to one, two, and three unit cells, respectively. It can be seen that when the OH^- group is within three unit cells from the vacancy, there is a significant drop in the MSD compared to the IVAC only simulation. To make sure that we observe a real trend of the MSD slope, and not simply random effects, we repeated several simulations by using different seeds of the random number generator, which correspond to different initial positions and velocities of the iodide ions, and indeed, the trend was confirmed. This is because the vacancy migration tends to go toward the OH^- group and once it is within one unit cell distance, the migration of the IVAC is blocked.We have shown that when an iodide vacancy defect is formed in the material, another iodide atoms will migrate to fill the vacancy, consequently creating a new vacancy in its place. This process will continue throughout the simulation domain until the vacancy reaches the boundary lines. However, in the presence of the hydroxyl group, the initial migration of iodide atoms will still occur, but, once the newly created vacancy is within roughly one unit cell from the hydroxyl group, this group will migrate toward the vacancy and will remain very close to it, or possibly fill it itself. Thus, the

hydroxyl is capable of stopping the migration of the iodide and allowing the system to return to stability(see Fig.21).

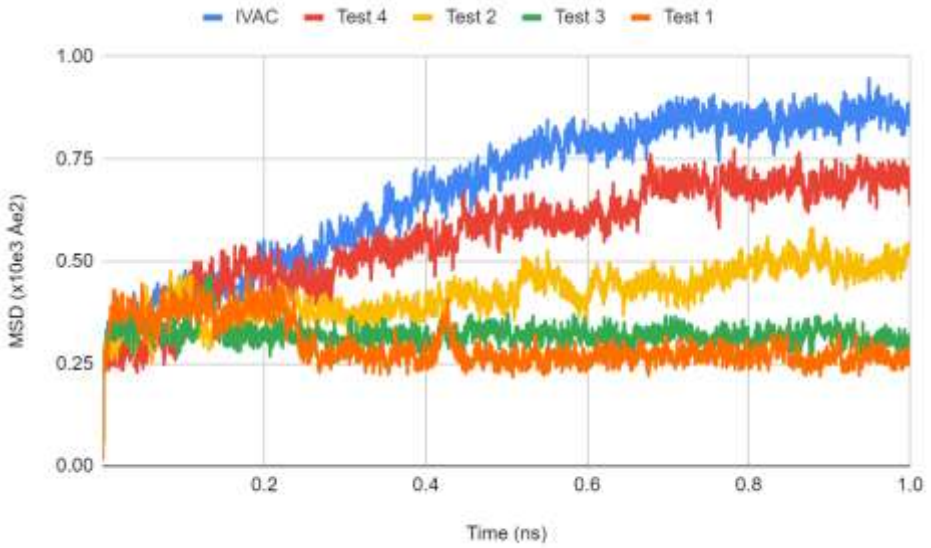

Figure 20. *MSD of all atoms at 300K for 1 ns. From ascending order, each test represents the vacancy and OH^- group are initially placed further apart. In Test 1 they are placed within the same unit cell, in Test 2 they placed one unit cell apart, and so on. The IVAC case corresponds to the MSD of all atoms without the addition of the OH^- group.*

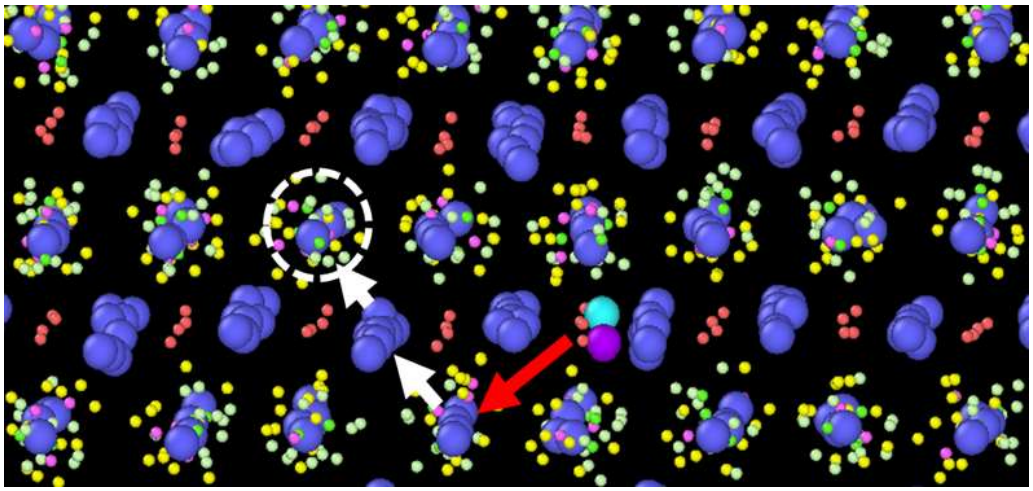

Figure 21. *An example of migration path of both the iodides (white arrows) and hydroxyl group (red arrow) in the presence of a vacancy. The initial position of the iodide vacancy is indicated by the dashed circle. The iodides are shown as dark blue spheres, and the OH^- as a light blue-violet group.*

In Figure 21 the white dashed circle indicates the initial placement of the IVAC, and the white arrows show the path of the iodides that have migrated and created new vacancies behind them. The red arrow indicates the migration of the hydroxyl group that has joined with the final vacancy, stopping the migration.

With respect to **MS6** (Well defined protocol for PSC characterization and for extracting the accurate value for PCE) we assemble a procedure to be implemented for obtaining a proper PCE:
- Stabilize V_{oc}; Avoid pre-poling the sample with either $V>V_{oc}$ or $V<0$
- Consider continuous R-Fw bias scans- otherwise the two scan shall not be correlated
- Calculate the hysteresis index
- Reduce the bias can rate until the R and Fw scans match (ideally)

- **D16. Report on the performances of PV modules, comparison with the market – (P4)**

First attempts in fabricating PV modules were made in 2022. Since then, the printing technology was improved for increasing both, the performance and homogeneity of large area PSCs. With the optimizations made in 2023 we obtained a very good homogeneity and a better PCE. Examples of the J-V characteristics on stabilized large area PSCs in PV-modules fabricated during 2023 (as those depicted in Fig.3, of 2.4 cm^2 area) are given in Fig. 22. From 9 such mini-panels, 15x15 cm^2 PV glass protected panels were fabricated (**MS8**) and they are able to power small devices toy-like devices as windmill, cars, boats. The stabilized PCE of these panels is still low to be competitive. In fact, there are yet no PSCs based PV panels available on the market indicating that are still important issues to be solved.

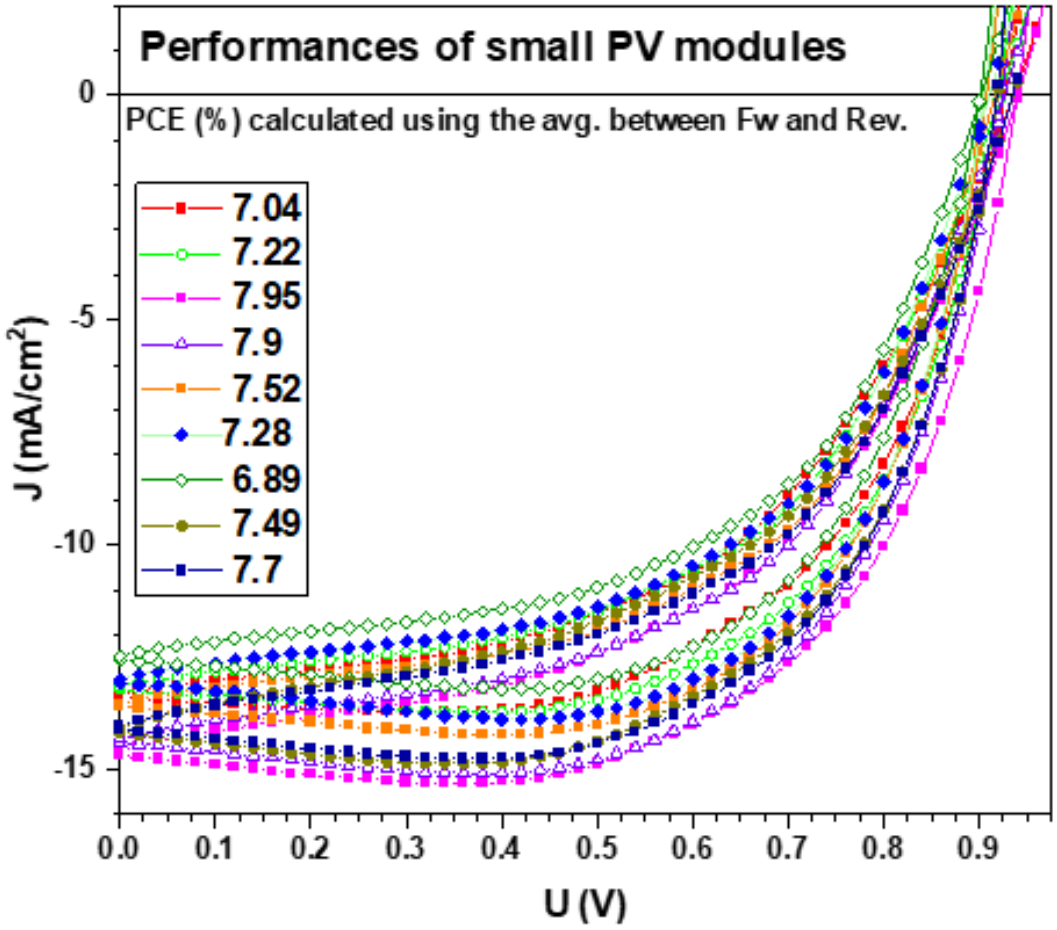

***Figure 22**. J-V characteristics and the corresponding PCE of large area PSCs (2.4 cm^2) in the 5 x5 cm^2 PV mini-modules.*

Details on the exploitation and dissemination of the results

- **presenting invited, oral or poster contributions during participation in international conferences (4 contributions):**

1) **Oral presentation**: ***Insights on the degradation of perovskite solar cells from bias stress tests***, N. Filipoiu, A. T. Preda, C. A. Pantis-Simut, D.V. Anghel, R. Patru, A. G. Mirea, M. Florea, C. Besleaga, I. Pintilie, A. Manolescu, G. A. Nemnes, 21st International Balkan Workshop on Applied Physics and Materials Science, Constanta, 11-14 iulie 2023, https://ibwap.ro/wp-content/uploads/2023/06/Accepted-Abstracts-IBWAP-2023.pdf (pg. 3)

2) **Poster presentation**: ***Investigation of the band alignment in mixed halide perovskite- Cu2O interfaces***, N. Filipoiu, C. A. Pantis-Simut, M. Cuzminschi, D. V. Anghel, G. E. Stan, C. Besleaga, I. Pintilie, K. Torfason, A. Manolescu, G. A. Nemnes, **21st International Balkan Workshop on Applied Physics and Materials Science, Constanta, 11-14 iulie 2023** , https://ibwap.ro/wp-content/uploads/2023/06/Accepted-Abstracts-IBWAP-2023.pdf (pg. 5)

3) **Oral presentation**: ***OH^- ions can reduce the iodide migration in MAPI***, R. E. Brophy, M. Kateb, I. Ghitiu, N. Filipoiu, K. Torfason, H. G. Svavarsson, G. A. Nemnes, I. Pintilie, A. Manolescu, **International Semiconductor Conference (CAS), Sinaia,11-13 octombrie, 2023**, https://ieeexplore.ieee.org/document/10303698 , DOI: 10.1109/CAS59036.2023.10303698

4) **Invited talk** at **Device physics characterization and interpretation in perovskite and organic materials (DEPERO) Conference,3-5 Octombrie 2023**: "***Capacitive and inductive effects in perovskite solar cells***", G. A. Nemnes , N. Filipoiu , A. T. Preda , D. V. Anghel , R. Patru R. E. Brophy , M. Kateb , C. Besleaga , A. G. Tomulescu , I. Pintilie , A. Manolescu, https://www.nanoge.org/DEPERO/general-information , https://www.nanoge.org/DEPERO/program-info/program

- **publishing research articles in scientific journals (3 articles):**

1) ***Partial replacement of Pb^{2+} in $MAPbI_{2.6}Cl_{0.4}$ perovskite films and their photovoltaic performance,*** S. Derbali, K. Nouneh, L.N. Leonat, V. Stancu, A. G. Tomulescu , A. C. Galca, M. Ebn Touhami, I. Pintilie, M. Florea, ***Journal of Materials Science: Materials in Electronics 34, 903 (2023).*** *https://doi.org/10.1007/s10854-023-10318-9*

2) ***Effect of Pressure on the Dynamics of Iodide Defects in Methylammonium Lead Iodide: An Atomistic Simulation****,* R. E. Brophy, M. Kateb, K. Torfason, G. A. Nemnes, H. G. Svavarsson, I. Pintilie and Andrei Manolescu, ***J. Phys. Chem. C 127, 7938 (2023*)**, *https://doi.org/10.1021/acs.jpcc.3c00657* , Free submitted from repository https://doi.org/10.48550/arXiv.2302.05696

3) ***Sub-stochiometric nickel oxide hole selective contacts in solar cells; comparison of simulations and experiments with sputtered films***. M. Nayak, K. Bergum, G. Stan, I.H. Lee and A. Kuznetsov, ***Physica Status Solidi A,*** 220: 2200651 (2023). *https://doi.org/10.1002/pssa.202200651*

- **20-25 pages brochures with the yearly results and activities of the project,** distributed during workshops and Conferences and via the web page of the project

- **Organizing visits and "hands-on" experiments for pupils and teachers** showing the printing technologies used in the project, perovskite solar cells and their utility (powering several small toy-like devices as windmill, cars, boats) during the **"Scoala Altfel"** (in February, March, April and November 2023) and "**Noaptea cercetatorului"** https://noapteacercetatorilor.educatiepentrustiinta.ro/, Septembrie 2023 events

Towards perovskite large area photovoltaics

Project code:	EEA-RO-NO-2018-0106 (SEE-36)
Project acronym:	PERLA-PV
Duration:	01.01.2021 – 30.04.2024
Total budget from the Programm (euro):	1,177,533.00
- Grant (85%):	1,000,903.05
- Co-financing (15%):	176,629.95
Own budget (euro):	146,010.00
Project Webpage:	http://perla-pv.ro/
Project Promoter organization:	INCDFM
Principal Investigator:	Ioana Pintilie
Project Partner organization (1):	Universitatea Oslo
Project Partner organization (2):	Universitatea Reykjavik
Project Partner organization (3):	IFIN-HH
Project Partner organization (4):	WATTROM -Tritech Group SRL

The EEA Grants represent the contribution of Iceland, Liechtenstein and Norway towards a green, competitive and inclusive Europe.

There are two overall objectives: reduction of economic and social disparities in Europe, and to strengthen bilateral relations between the donor countries and 15 EU countries in Central and Southern Europe and the Baltics.

The three donor countries cooperate closely with the EU through the Agreement on the European Economic Area (EEA). The donors have provided €3.3 billion through consecutive grant schemes between 1994 and 2014. For the period 2014-2021, the EEA Grants amount to €1.55 billion. The priorities for this period are: 1) Innovation, Research, Education and Competitiveness; 2) Social Inclusion, Youth Employment and Poverty Reduction; 3) Environment, Energy, Climate Change and Low Carbon Economy; 4) Culture, Civil Society, Good Governance and Fundamental Rights; 5) Justice and Home Affairs